

Contents lists available at ScienceDirect

Journal of Quantitative Spectroscopy & Radiative Transfer

journal homepage: www.elsevier.com/locate/jqsrt



Line mixing and broadening in the $v(1\rightarrow 3)$ first overtone bandhead of carbon monoxide at high temperatures and high pressures



Fabio A. Bendana*, Daniel D. Lee, Chuyu Wei, Daniel I. Pineda, R. Mitchell Spearrin

Department of Mechanical and Aerospace Engineering, University of California, Los Angeles (UCLA), Los Angeles, CA 90095, USA

ARTICLE INFO

Article history:
Received 11 June 2019
Revised 2 August 2019
Accepted 2 September 2019
Available online 5 September 2019

Keywords:
Line mixing
Line broadening
Absorption spectroscopy
CO
High pressure
High temperature

ABSTRACT

Temperature-dependent line mixing and line broadening parameters were empirically-determined for 17 rovibrational transitions in the $v(1\rightarrow 3)$ bandhead of carbon monoxide near 2.3 μ m. Collisional effects on the high rotational energy lines ($E''=5500-8600\,\mathrm{cm}^{-1}$) in the R-branch were studied over a range of temperatures from 1200–3750 K in a shock tube and heated gas cell. Measured spectra comprising the target lines in Ar and CO bath gases were fit with Voigt profiles at near-atmospheric pressures to determine line-broadening coefficients, with temperature dependence accounted by a power law. With line broadening established, line-mixing effects were examined at elevated pressures up to 60 atm at similar temperatures, reflecting conditions in high-pressure combustion environments. A modified exponential gap model for line mixing was developed to capture the pressure and temperature dependence of collisional transfer rates for the bandhead region using the relaxation matrix formalism.

© 2019 Elsevier Ltd. All rights reserved.

1. Introduction

Carbon monoxide (CO) is an important molecule in both atmospheric and combustion chemistry. Absorption spectroscopy of CO is relevant in ground-based measurements (e.g. smog regulations) of on-road vehicle emissions [1], satellite-based remote sensing of pollutants for climate science [2], time-resolved characterization of combustion dynamics [3], and thermal radiation modeling in the development of planetary entry and propulsion systems [4]. In all such cases, accurate spectroscopic data with appropriate thermodynamic scaling across relevant conditions provide a basis for quantitative simulation and analysis. This work experimentally investigates the CO spectra near 2.3 µm at high-temperature conditions relevant to combustion and planetary entry over a broad range of pressures (up to 60 atm), with the goal of developing an accurate model of the target spectral domain capturing relevant collisional effects.

Notably, the first overtone band of CO near 2.3 μ m has been utilized extensively for combustion gas sensing via laser absorption methods. Several works have targeted rovibrational transitions in the $\nu(0\rightarrow2)$ band for CO measurements to monitor syngas composition (T < 400 K, P < 20 atm) [5] and combustion-based power plant exhausts (T < 1200 K, P \sim 1 atm) [6]. More

E-mail addresses: fbendana@ucla.edu (F.A. Bendana), daniellee9101@ucla.edu (D.D. Lee), weicy@ucla.edu (C. Wei), dipineda@ucla.edu (D.I. Pineda), spearrin@ucla.edu (R.M. Spearrin).

recently, this domain was exploited by our group for in-chamber rocket combustion gas sensing at much higher temperatures and pressures (T > 3000 K, P > 100 atm) [7,8]. At these extreme combustion temperatures, transitions with higher rotational energies and vibrational hot bands, such as the $v(1\rightarrow 3)$ band, become more prominent. Moreover, at such extreme combustion conditions, transitions comprising the bandhead regions exhibit local absorption peaks with high differential absorption, attractive for sensing. At high gas densities, spectrally crowded bandhead regions become susceptible to collisional line mixing [9]. In this work, we examine line broadening and mixing in argon and carbon monoxide bath gases for 17 high-energy transitions (J'' = 42-58) near the $v(1\rightarrow 3)$ bandhead of CO, identified in Fig. 1.

Line broadening of carbon monoxide has been shown to have weak vibrational energy dependence, with stronger dependence on rotational energy. Though much progress has been made in quantifying and modeling CO line broadening in the $v(0\rightarrow1)$ [10–12], $v(0\rightarrow2)$ [11,13–18], and $v(0\rightarrow3)$ [19–21], a dearth of line-broadening data exist for rotational quantum number transitions larger than J''>31 of any vibrational band, as noted in Fig. 2. This is primarily because most measurements of line broadening coefficients for CO have been conducted at or near room temperature [17,22], corresponding to the lower rotational energy transitions. We focus this experimental study to a temperature range of 1200–3750 K to access lines with higher rotational energies.

Line mixing is a band narrowing effect that occurs at high pressures, resulting from local population transfers when collisional linewidths are on the order of line spacing [23]. Line mixing is

^{*} Corresponding author.

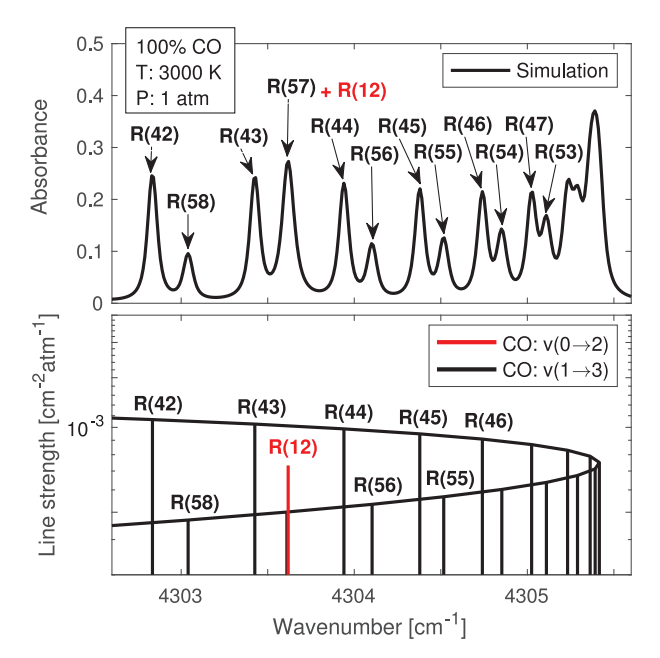


Fig. 1. (*top*) Spectral absorbance simulation of the $v(1 \rightarrow 3)$ first overtone bandhead of CO at 3000 K and 1 atm for pure CO. (*bottom*) Line strength positions and magnitudes of the spectral transitions relevant to this work.

often observed in bandheads where line spacing becomes very small. Q-branches that have bandheads at lower rotational energies are often observed to have line mixing near ambient temperatures [23]. Here we study line mixing in the R-branch bandhead of the $v(1\rightarrow 3)$ overtone band of CO at pressures up to 60 atm. A spectral simulation of the target bandhead considered herein is shown in Fig. 1.

This paper describes the experimental measurements and modeling of the aforementioned line broadening and mixing effects in the $v(1\rightarrow 3)$ first overtone bandhead of CO at high temperatures and high pressures, with Ar and CO collision partners. After establishing the theoretical framework, we present our experimental methods, including the optical setup, experimental apparatus, and data processing techniques required to obtain broadening parameters from laser absorption measurements at moderate pressures (P < 2.5 atm). We then discuss how these broadening parameters were used to develop the complimentary line-mixing model based on high-pressure (up to 60 atm) spectrally-resolved CO absorption measurements in a shock tube. The combination of broadening and mixing models provides a basis for spectral simulation of CO near 2.3 μ m over a broad range of temperatures and pressures.

2. Theory

2.1. Absorption spectroscopy and line broadening

The basic theory of laser absorption spectroscopy is detailed thoroughly in the literature [24], but a brief review is provided here for context and nomenclature definitions. The transmission τ_{ν} of monochromatic light at frequency ν through an absorbing gas medium can be expressed by the Beer–Lambert law in Eq. (1):

$$\tau_{\nu} = \left(\frac{I}{I_0}\right)_{\nu} = \exp(-\alpha_{\nu}) \tag{1}$$

where I_0 and I are the incident and transmitted light intensities, respectively, and α_{ν} is the spectral absorbance. In the spectral vicinity of *a single transition*, the spectral absorbance relates to

thermophysical gas properties through Eq. (2):

$$\alpha_{\nu} = -S(T)NL\phi(\nu) \tag{2}$$

where S(T) [cm⁻¹/(molec · cm⁻²)] is the line strength of the transition, L [cm] is the path length, $\phi(\nu)$ [cm] is the line shape function, and N [molec · cm⁻³] is the total number density of the absorbing species, given by:

$$N = \frac{PX}{k_B T} \cdot 10^{-6} \tag{3}$$

Here, P is the pressure with units of [Pa], X is the mole fraction of the absorber, k_B [J/K] is the Boltzmann constant, and T [K] is the temperature. Based on the compressibility factors for CO and Ar, deviations from the ideal gas assumption implied in Eq. (3) are not expected to exceed 1% for any condition in this study [25]. The spectral line shape $\phi(\nu)$ can be modeled using a Voigt profile [23], a convolution of a Lorentzian and a Gaussian profile accounting for collisional and Doppler broadening, respectively. Each broadening mechanism is characterized by full width at half maximum (FWHM) parameter; $\Delta \nu_C$ [cm $^{-1}$] for collisional broadening and $\Delta \nu_D$ [cm $^{-1}$] for Doppler broadening. Doppler linewidth is given by Eq. (4) [24]:

$$\Delta \nu_D = \nu_0 (7.1623 \cdot 10^{-7}) \sqrt{\frac{T}{M}} \tag{4}$$

where v_0 [cm⁻¹] is the transition linecenter and M [g·mol⁻¹] is the molecular weight of the absorbing species. Collisional linewidth scales with the collision frequency of the absorbing molecule A, adjusted for quantum state, and is often modeled as the product of pressure and the sum of mole fraction weighted collisional broadening coefficients of each perturbing species B, as shown in Eq. (5):

$$\Delta \nu_{C} = P \sum_{B} X_{B} 2 \gamma_{A-B}(T) \tag{5}$$

where $\gamma_{A-B}(T)$ [cm⁻¹atm⁻¹] is the transition-dependent collisional broadening coefficient at temperature T. Note that in Eq. (5), total pressure P has units of [atm].

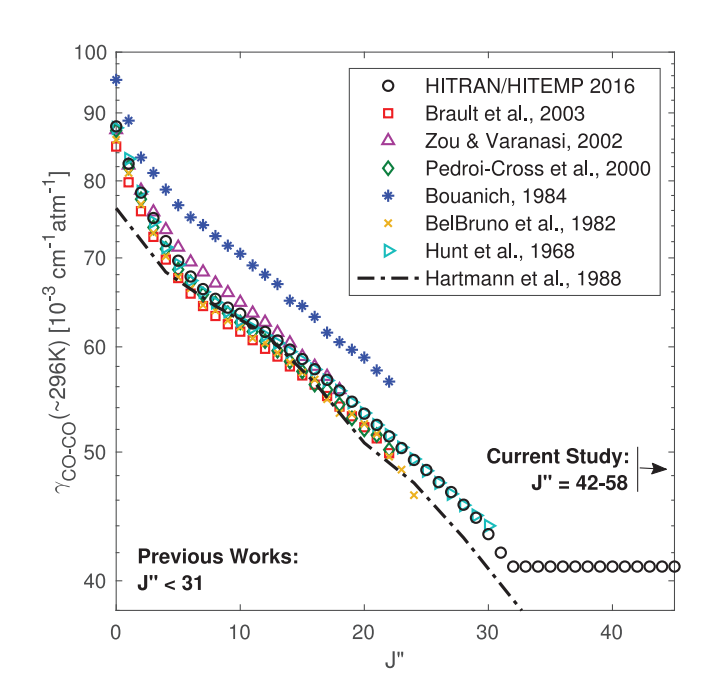


Fig. 2. Experimental self-broadening coefficients for CO transitions obtained by previous works. The current study focuses on higher rotational quantum number transitions (J'' = 42-58) to extend diagnostic capabilities at extreme temperatures and pressures.

As seen in Eq. (5), collisional broadening scales linearly with pressure and often leads to an additive blending of neighboring lines. The temperature dependence of $\gamma_{A-B}(T)$ is modeled as a power law expression, given in Eq. (6):

$$\gamma_{A-B}(T) = \gamma_{A-B}(T_0) \left(\frac{T_0}{T}\right)^n \tag{6}$$

where $\gamma_{A-B}(T_0)$ [cm⁻¹atm⁻¹] is the broadening coefficient at a reference temperature T_0 , and n is the line-specific temperature exponent of the absorbing species. As lines become more closely spaced together, the spectral absorbance α_{ν} at a given wavenumber ν is no longer a function of just one spectral transition, but is rather a summation of all neighboring transitions as demonstrated in the bandhead shown in Fig. 1. In this work, we report measured values of $\gamma_{\rm CO-CO}$ and $\gamma_{\rm CO-Ar}$ at a reference temperature of 1500 K along with their respective temperature exponents, $n_{\rm CO-CO}$ and $n_{\rm CO-Ar}$, for 17 transitions in the $\nu(1\rightarrow 3)$ band of CO (described in Section 1). The reported values are considered most appropriate for a temperature range of 1500–4000 K.

2.2. Line mixing

Line mixing relates to collisions that cause a change in rotational energy, usually within the same vibrational energy level. At high gas densities and collision frequencies, the collision-induced population transfers between rotational energy states can cause a vibrational band narrowing effect due to an intensity exchange between different lines [23]. This effect is more pronounced in spectrally dense regions, such as bandheads, where line spacing is small.

To illustrate this phenomenon, consider two rovibrational transitions depicted in Fig. 3:

$$(v'',J'') \rightarrow (v',J')$$

and

$$(v'', K'') \rightarrow (v', K')$$

located at frequencies $v_{J'' \to J'}$ and $v_{K'' \to K'}$, respectively, where J and K denote different rotational energy levels for the diatomic. In the presence of radiation, a molecule in energy level (v'', J'') can be excited to (v', J') by a photon at frequency $v_{J'' \to J'}$. Additionally, a molecule in energy level (v'', J'') can be transferred to energy level (v'', K'') via collisions, then be excited to level (v', K') by absorbing a photon at frequency $v_{K'' \to K'}$, and finally relax from (v', K') to (v', J') via collisions [23]:

$$(v'', J'') \rightarrow (v'', K'') \rightarrow (v', K') \rightarrow (v', J')$$

This path from (v'', J'') to (v', J') via (v'', K'') and (v', K') shows that a molecule initially at (v'', J'') can contribute to the absorption intensity located at $v_{K'' \to K'}$ by population transfers between energy states associated with collisions. Population transfers of the reverse path are also possible.

For collision-induced population transfers to have a significant effect on the vibrational band structure (i.e. transfer intensity between line positions), the following criteria must generally be satisfied as described in [23]: (1) The neighboring transitions must be from the same species; (2) the transitions must be similar in upper and lower state energy levels, such that transfers are purely rotational jumps; (3) the transitions must be identical in nuclear spin; (4) collision broadened linewidths are greater than line spacing, $|v_{J'' \to J'} - v_{K'' \to K'}| < \Delta v_C$. This last criterion reflects the scaling with gas density and collision frequency. Accordingly, at very high gas densities or pressures, line mixing can significantly affect the intensity distribution of a vibrational band.

To model line-mixing effects, we implement the relaxation matrix formalism [26] to account for collisional effects on the molecular spectra. For brevity, lower state rotational energy levels, J'' and

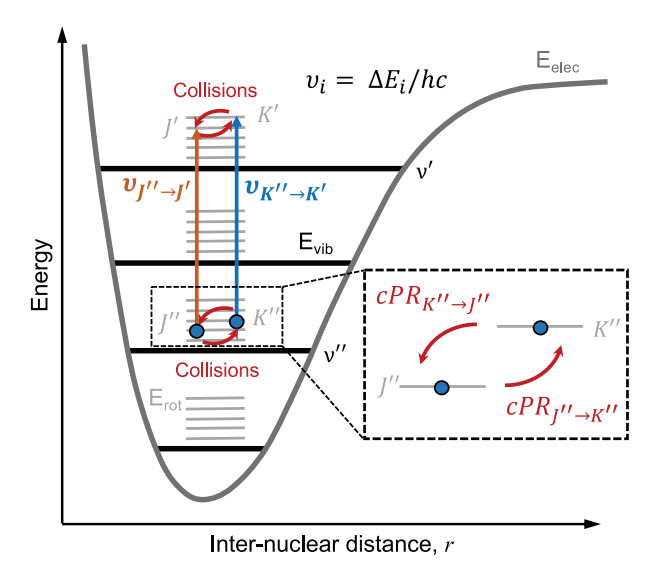


Fig. 3. Collisional line mixing of rovibrational transitions in an overtone band of a diatomic molecule, adapted from Hartmann [23].

K'', are written as J and K for the proceeding equations. The absorbance, α_{ν} , for overlapping transitions can be written within the impact approximation [27] in the following form:

$$\alpha_{\nu} = \frac{NL}{\pi} \operatorname{Im}(\mathbf{d} \cdot \mathbf{G}^{-1} \cdot \boldsymbol{\rho} \cdot \mathbf{d}) \tag{7}$$

where ρ is a diagonal matrix with nonzero elements ρ_J defined by the lower state Boltzmann population fraction [28]:

$$\rho_J = \frac{N_J}{N} = \frac{g_J''}{O} \exp\left(-\frac{hcE_J''}{k_B T}\right) \tag{8}$$

where N_J [molec \cdot cm⁻³] is the number density, g_J'' is the lower state degeneracy, E_J'' [cm⁻¹] is the lower state energy, Q is the total internal partition function, h [J \cdot s] is Planck's constant, and c [cm/s] is the speed of light. **d** [cm⁻¹/(molec \cdot cm⁻²)] $^{\frac{1}{2}}$ is a vector of transition amplitudes with elements d_I given as [29]:

$$d_J = \sqrt{\frac{S_J(T)}{\rho_J}} \tag{9}$$

Another commonly used form of Eq. (7) is shown in Appendix A, where the temperature dependence of ${\bf d}$ is removed. The dependence on wavenumber ν [cm $^{-1}$] in Eq. (7) is within ${\bf G}$ [cm $^{-1}$], a complex matrix defined as:

$$\mathbf{G} = \nu \mathbf{I} - \mathbf{H} \tag{10}$$

where I is the identity matrix and a frequency-independent matrix H [cm⁻¹] is defined as:

$$\mathbf{H} = \mathbf{v}_0 - iP\mathbf{W} \tag{11}$$

 v_0 [cm⁻¹] is a diagonal matrix of transition frequencies and **W** [cm⁻¹/atm] is the relaxation matrix [26]. Note that in Eq. (11), total pressure P is in units of [atm]. **H** can be diagonalized using a similarity transform [30] to obtain a diagonal eigenvalue matrix Ω [cm⁻¹] with diagonal elements ω_I [cm⁻¹] such that:

$$\mathbf{\Omega} = \mathbf{A}^{-1} \cdot \mathbf{H} \cdot \mathbf{A} \tag{12}$$

Since **G** only differs from **H** by a constant diagonal matrix, \mathbf{G}^{-1} is also diagonalized by **A**. Eq. (7) can now be written as a function of ν spanning all relevant spectral transitions J:

$$\alpha_{\nu} = \frac{NL}{\pi} \operatorname{Im} \left[\sum_{J} \frac{(\mathbf{d} \cdot \mathbf{A})_{J} (\mathbf{A}^{-1} \cdot \boldsymbol{\rho} \cdot \mathbf{d})_{J}}{(\nu - \omega_{J})} \right]$$
(13)

The relaxation matrix is implemented to model line-mixing effects in the spectra and is given by:

$$\mathbf{W}_{JK} = \begin{cases} \gamma_J + i\Delta \nu_{0,J} & \text{if } J = K \\ -R_{J \to K} & \text{if } J \neq K \end{cases}$$
 (14)

where the real diagonal elements of **W** are the broadening coefficients γ_J discussed in Section 2.1 and the imaginary diagonal elements are the pressure shifts $\Delta\nu_{0J}$ [cm⁻¹/atm] (termed " δ " in the HITRAN database [31]). The real off-diagonal elements represent the state-specific population transfer rates, $R_{J\to K}$ [cm⁻¹/atm], between two states, J and K. Notably, for linear molecules, broadening coefficients can also be expressed in terms of total depopulation rates through Eq. (15) [23].

$$\gamma_{J} = \sum_{I \neq K} R_{J \to K} \tag{15}$$

The imaginary off-diagonal components of **W** represent contributions from rotational dephasing [32]. Previous work has found the effect of these terms to be negligible for collisionally-narrowed infrared spectra at both low and high densities [33]. Consequently, the rotational dephasing contributions are approximated as zero for all transitions in the relaxation matrix. It is noteworthy that if the population transfer rates are set to zero for all transitions, Eq. (7) simply represents the sum of the Lorentzian lines with no line-mixing effects. When multiple collision partners are present, the full relaxation matrix is written as a summation of the individual perturber contributions:

$$\mathbf{W} = \sum_{B} X_{B} \mathbf{W}_{A-B} \tag{16}$$

In this study, we model $R_{J \to K}$ using a modified-exponential-gap (MEG) law [34,35] to construct the real part of the relaxation matrix. The MEG law takes the following form:

$$R_{J \to K} = a_1(T) \left[\frac{1 + a_4 \left(\frac{E_J''}{a_2 k_B T} \right)}{1 + a_4 \left(\frac{E_J''}{k_B T} \right)} \right]^2 \times \exp \left[\frac{-a_3 \left(E_K'' - E_J'' \right)}{k_B T} \right]$$
(17)

where $a_1(T)$ [cm⁻¹/atm], a_2 , and a_3 are species-specific MEG law coefficients obtained by fitting measured absorbance data to the model using a least-squares fitting routine. a_4 describes the collision duration [34] based on distance of closest approach [36] and is set to $a_4=2$ as an estimate for CO–CO collisions [37,38]. It is important to note that the value of a_4 is not critical in the ability of the MEG law to fit the measurement data [37,38]; therefore, it was kept constant for all experiments in this study.

This empirically-derived MEG law formulation has been successfully implemented for other linear molecules [28,37] using absorption spectroscopy techniques to account for line mixing. Since collisions promote the Boltzmann population distribution, the upward and downward population transfer rates, $R_{J \to K}$ and $R_{K \to J}$, respectively, can be related through the detailed-balance principle [39]:

$$\rho_K R_{K \to J} = \rho_J R_{J \to K} \tag{18}$$

This completes the real part of the relaxation matrix and indicates that starting from the less populated energy level is the more probable of the two counter processes. This suggests that line mixing favors population transfers from weak transitions to strong transitions, inducing a narrowing of the spectral structure and enhancing high absorbing regions.

Only a single set of measured absorbance data is needed to obtain the species-specific MEG law coefficients for a given temperature [40]. To determine the temperature dependence of the population transfer rates, $a_1(T)$ can be modeled as a power law expres-

sion

$$a_1(T) = a_1(T_0) \left(\frac{T_0}{T}\right)^m$$
 (19)

where we define a temperature exponent m obtained by fitting multiple sets of absorbance data at different temperatures, and $a_1(T_0)$ is the MEG law coefficient at a reference temperature T_0 .

Similar to the reported broadening coefficients $\gamma_{\text{CO}-B}$, we report measured values of MEG law coefficients for both $a_{i,\text{CO}-\text{CO}}$ and $a_{i,\text{CO}-\text{Ar}}$ with their respective temperature exponents, $m_{\text{CO}-\text{CO}}$ and $m_{\text{CO}-\text{Ar}}$ at a reference temperature of 1500 K. We show that these parameters can model line-mixing effects in the $\nu(1\rightarrow 3)$ bandhead of CO at high pressures (> 5 atm) over a temperature range of 2000–3600 K.

3. Experimental setup

We first note that extreme caution should be exercised when handling mixtures with high concentrations of CO, due its acute toxicity. All CO was stored in a ventilated toxic gas cabinet and transported to the experimental apparatuses in lines that had been thoroughly checked for leaks with inert gases. After each measurement, each device described in this section was vacuumed and diluted with N_2 to eliminate residual CO before the next measurement.

The experiments in this work were conducted using the highenthalpy shock tube facility illustrated in Fig. 4 with some supporting collisional broadening measurements conducted in a heated static optical gas cell described in previous work [41]. The shock tube has a constant 10.32 cm inner diameter, a 4.88 m long driven section, and a 1.56 m long driver section. The test section is circumscribed with interchangeable port plugs, which integrate different sensors or optical windows, located ~ 2 cm from the driven endwall. Incident shock speeds are determined by five fast-response, piezoelectric time-of-arrival sensors (Dynasen, Inc.) located at equidistant intervals over the last 170 cm of the driven section, as shown in the bottom of Fig. 4. Initial reflected shock conditions are determined by the incident shock speed with a typical uncertainty of $\sim 1\%$ in temperature when properly accounting for vibrational relaxation of the gas mixture [42]. Prior to each experiment, a roughing pump (Alcatel Adixen 2021i) was used to vacuum down the shock tube to $< 1 \times 10^{-3}$ Torr. Test gas mixtures were barometrically prepared in a 12.5 L agitated mixing tank using a heated capacitance manometer (MKS 627D Baratron) with a full-scale pressure range of 1000 Torr and an uncertainty of 0.12% of the reading. All gases were supplied by Airgas, Inc. with purity levels of 99.9% for CO, 99.999% for Ar, and 99.995% for He. Two different mixtures were prepared for collisional broadening and line mixing investigations: 100% CO for CO-CO measurements and 30% CO/Ar for CO-Ar measurements.

The $v(1\rightarrow 3)$ bandhead of CO near 2.3 µm was spectrally resolved by current-tuning a continuous-wave distributed-feedback (DFB) laser (Norcada, Inc.) with ~ 10 mW output power. The DFB laser is temperature- and current-tunable from 4290–4325 cm⁻¹. A 10 kHz triangle waveform, shown in Fig. 4, was implemented to injection-current-tune the light source over a wavenumber range of $\sim 4.5~\text{cm}^{-1}$ between 4302–4306.5 cm⁻¹. Additionally, the injection current was scanned below the lasing threshold to account for transient thermal emission during the measurements. The relative frequency of the laser light during the scan was determined using a germanium etalon with a free spectral range of 0.0231 cm⁻¹. During the experiments, the incident light was pitched across the shock tube through two 0.5° wedged sapphire windows with a 9.5 mm aperture, as shown in Fig. 4. The transmitted light was passed through a bandpass spectral filter (Spectrogon, 2320 ± 20 nm) and an iris to mitigate thermal emission,

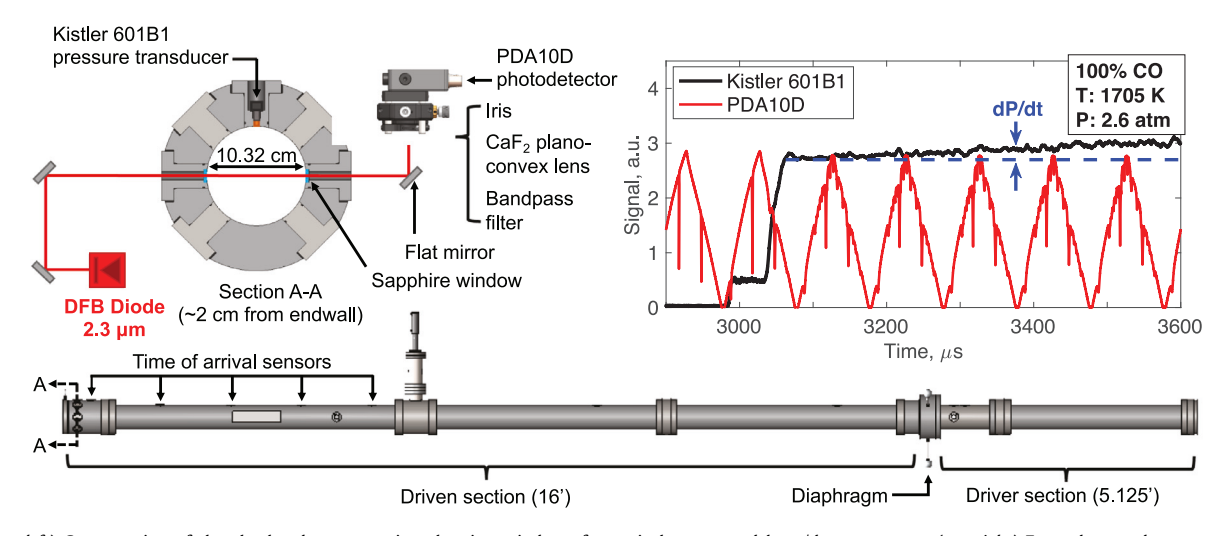


Fig. 4. (top left) Cross-section of the shock tube test section showing windows for optical access and laser/detector setup. (top right) Example raw detector and pressure transducer signals during non-reactive shock heating of pure CO. (bottom) Side view of the shock tube showing lengths of the driven and driver sections as well as the locations of the time-of-arrival sensors.

and was focused onto a thermo-electrically cooled photodetector (Thorlabs PDA10D) using a CaF₂ plano-convex lens. Incident and reflected shock pressures were measured using a dynamic pressure transducer (Kistler 601B1) mounted in one of the test section port plugs, which was connected to a charge amplifier (Kistler 5018A). Pressure and detector data were collected on a PicoScope 4000 series data acquisition module at 80 MHz while detector data were sampled at the maximum detector bandwidth of 10 MHz, yielding an equivalent measurement rate of 5 MHz.

Representative raw time-resolved signals from a shock tube experiment are shown in Fig. 4. Prior to the incident shock arrival, the R(12) feature from the $v(0\rightarrow 2)$ first overtone band of CO is visible at 296.3 K and 23.8 Torr. Following the passage of the incident and reflected shocks, R(42)–R(58) appear as the high temperatures more densely populate the $v(1\rightarrow 3)$ first overtone hot band. Throughout the test time, a non-ideal pressure rise was often observed and accounted for by assuming isentropic compression of the test gas. This method has shown to be a valid assumption for correcting thermodynamic conditions behind reflected shock waves [43]. For a single scan interval, the change in temperature and pressure are less than 0.3% and 1.2%, respectively, when pure CO was used, and 0.2% and 0.6% when the 30% CO/Ar mixture was used; thus, the thermodynamic properties were assigned at the scan mid-point and assumed to be constant during each scan.

Shock tube experiments for line-broadening parameters of pure CO were conducted over a temperature range of 1700-3750 K and a pressure range of 0.5-2.5 atm. Moderate pressures were targeted for line-broadening experiments to minimize spectral blending amongst neighboring transitions and resolve the line-specific broadening and temperature coefficients discussed in Section 2.1. For the 30% CO/Ar mixtures, the lower end of the temperature range was limited to 2000 K due to decreased absorption in the $v(1\rightarrow 3)$ band, precluding reliable line-broadening measurements; however, the pressure range (< 2.5 atm) was kept similar. Shockheated CO requires a finite amount of time to attain vibrational equilibrium; estimates of vibrational relaxation time for the mixtures used in these studies are shown in Fig. 5, with empirical correlations from Millikan and White [44]. Pure CO experiments have a faster vibrational relaxation time compared to CO/Ar mixtures, owing to argon's poor collision efficiency. Lower temperature (< 2500 K) line-broadening experiments were conducted at higher pressures (> 1.5 atm) to reduce vibrational relaxation time. At lower temperatures, reflected shock test times were typically

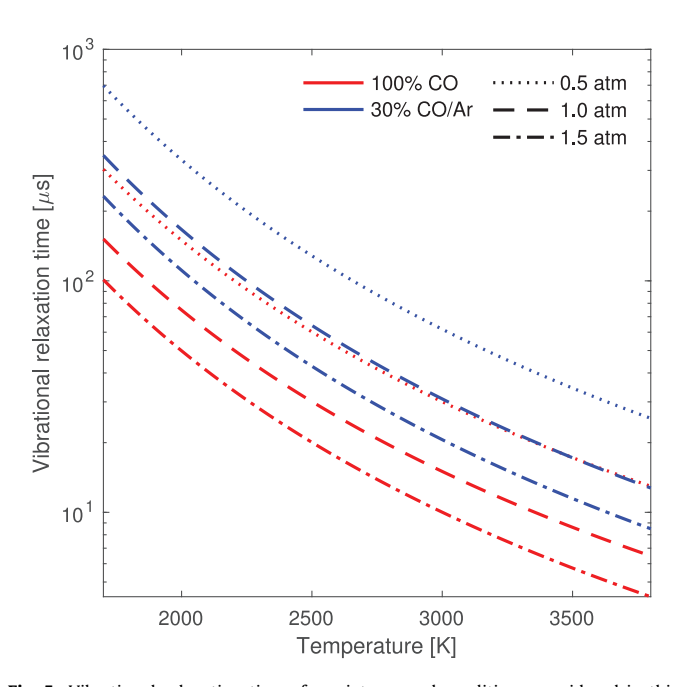


Fig. 5. Vibrational relaxation times for mixtures and conditions considered in this work, using calculations of Millikan & White [44].

 $\sim\!600~\mu s$, allowing sufficient time for CO to vibrationally relax. Processed laser scans were typically acquired at least 100 μs after the estimated vibrational relaxation time. Shock tube experiments for line-mixing parameters covered a temperature and pressure range of 2000–3600 K and 5–60 atm, respectively, for both pure CO and 30% CO/Ar. Higher pressures were targeted for line-mixing experiments in order to determine MEG law coefficients and prove pressure scalability.

For each experiment, absorbance α_{ν} was determined through Eq. (1) via measurements of incident and transmitted intensity, I_0 and I. The incident laser light intensity through the shock tube was measured without a mixture present prior to each shock experiment to provide a baseline I_0 for calculation of α_{ν} . Each scan of the transmitted laser intensity, I, was corrected for detector offset from both emission and dark current noise by tuning below the lasing threshold. Minimal emission was observed throughout the test,

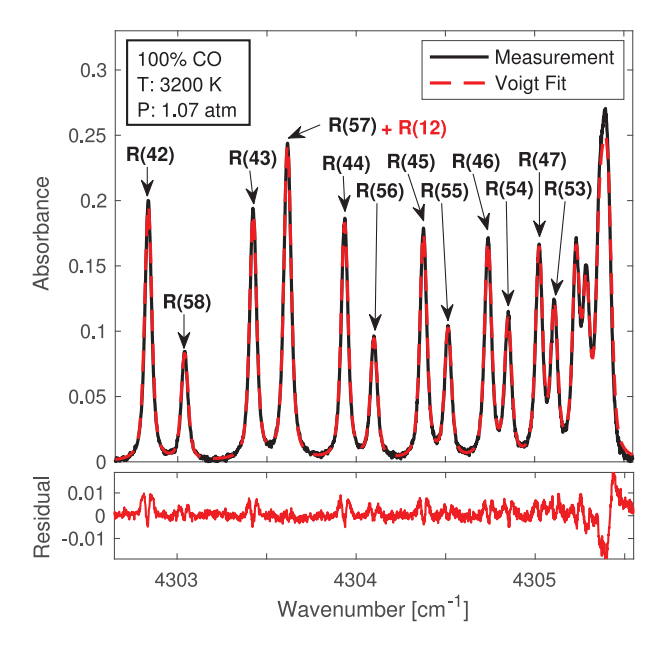


Fig. 6. (top) Absorbance of the first overtone bandhead of CO at 3200 K and 1.07 atm with corresponding Voigt fits. (bottom) Residuals of the Voigt fit, showing larger disagreement at the bandhead.

as seen in the representative data from Fig. 4. For broadening experiments, the absorbance profile was least-squared fit with Voigt lineshape functions positioned at the line center of each transition with the broadening coefficients set as the free parameters. For higher-pressure line-mixing experiments, the MEG law coefficients were set as free parameters with the diagonals of the relaxation matrix assigned with the pre-determined broadening coefficients.

4. Results and discussion

Temperature dependent line-broadening and line-mixing coefficients of CO with CO and Ar are reported for seventeen transitions in the $v(1\rightarrow 3)$ first overtone hot band between 4302–4306.5 cm $^{-1}$. Values for the transition line centers ν_0 , line strengths $S_J(T_0)$, and lower state energy levels E_J'' were taken from the HITEMP database [45]. Quantum number assignments and lower state energies are noted in Table 1. The following two subsections detail the line-broadening and line-mixing results, respectively.

4.1. Line broadening

Laser absorption measurements were made behind reflected shocks and in the heated optical cell to gather line broadening data from 1200–3750 K for R(42)–R(58). A representative single-scan absorbance measurement from a shock tube experiment with corresponding Voigt line fits is shown in Fig. 6. Generally, the Voigt fits produced low peak residuals (1–4%). At high temperatures and low pressures both CO-broadening and Ar-broadening experiments exhibited some evidence of collisional narrowing (gull-wing residual) likely due to a reduction in Doppler broadening from velocity-changing collisions [46]. Fig. 6 also provides evidence of line-mixing effects where the Voigt lineshape summation is unable to properly fit the measured absorbance near the bandhead.

As discussed previously, line-broadening experiments targeted lower pressures (< 2.5 atm) to minimize spectral blending from neighboring transitions, which become more significant near the bandhead and complicates the fitting routine. Despite the low pressures of the experiments, the R(48)–R(54) transitions near the bandhead are too closely spaced to reliably extract broadening in-

formation. Instead, the broadening coefficients from transitions before and after the bandhead–R(42)–R(47) and R(53)–R(58)–were used to establish a $J^{\prime\prime}$ dependency and estimate the broadening coefficients of the bandhead transitions for the Voigt line shape model

As previously mentioned, self-broadening measurements were conducted on a high-temperature gas cell at 1226 ± 10 K over a pressure range of 0.6-1.0 atm to extend the temperature range of the reported broadening parameters. This data served to reduce uncertainty in the temperature-dependence exponent, and to check that acquired data had negligible facility dependence. As with the shock tube measurements, the detectable transitions in the absorbance spectra were fit with simultaneous Voigt line shape functions positioned at the line center of each transition with broadening coefficient, $\gamma_{\text{CO}-B}(T)$, as the free parameter using a least squares fitting routine. Representative collision width measurements from these experiments are shown as a linear function of pressure in Fig. 7. At these lower temperatures (1226 \pm 10 K), the absorbance from each of the transitions after the bandhead was too weak (α_{ν} < 0.005) to recover reliable collision widths and was not factored into $\gamma_{CO-B}(T)$. Consequently, to help establish temperature dependence for the higher energy lines after the bandhead, R(53)-R(58), we incorporate estimates of roomtemperature broadening in the power law fit from an existing model [47] validated for lower J'' transitions [31]. The resulting broadening coefficients referenced to 1500 K and temperaturedependence exponents are reported in Table 1.

Owing to weak expected absorbance at the maximum temperatures achievable by the heated optical cell, CO–Ar broadening measurements were not conducted, considering these experiments would require significant dilution of the CO. Therefore, as with the aforementioned R(53)–R(58) lines in pure CO, a room-temperature estimation of the Ar-broadening coefficient [48] is incorporated into the power law fit for all transitions before and after the bandhead (R(42)–R(47) and R(53)–R(58)). Room-temperature Ar-broadening estimations were obtained by extrapolating existing measurements that have been validated at lower J" transitions [48].

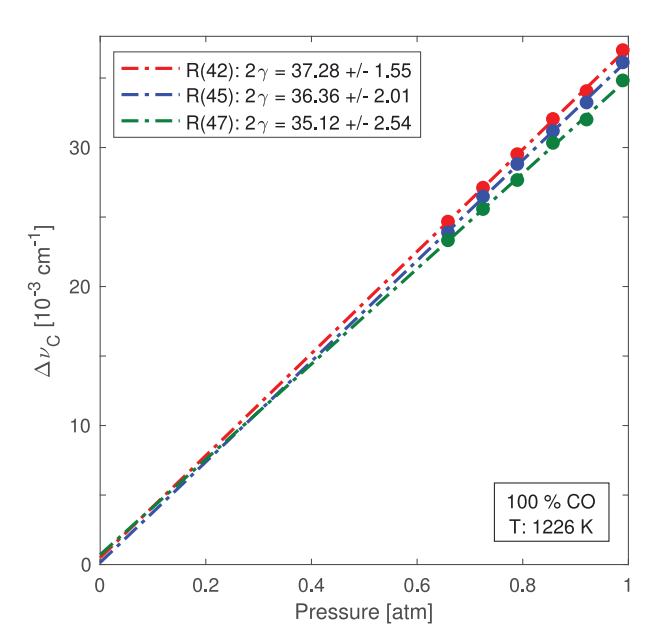


Fig. 7. Collisional width $\Delta \nu_C$ versus pressure for select rovibrational transitions in the $\nu(1{\to}3)$ first overtone bandhead recorded in the static optical cell at 1226 K. Measurements for R(42), R(45), and R(47) (markers) are shown along with best fits (dashed lines).

Table 1 Self- and Ar-broadened line parameters for the $v(1\rightarrow 3)$ band of CO.

Transition (v'', J'')	$E_J^{\prime\prime}$ [cm ⁻¹]	$\gamma_{\text{CO-CO}}(1500 \text{ K})$ [$10^{-3} \text{ cm}^{-1} \text{atm}^{-1}$]	$n_{\text{CO-CO}}$	$\gamma_{\rm CO-Ar}(1500 \text{ K})$ [$10^{-3} \text{ cm}^{-1} \text{atm}^{-1}$]	n _{CO-Ar}
R(1,42)	5563.82	17.08 ± 0.35^{a}	0.521 ± 0.023^{a}	12.36 ± 0.45^{b}	0.485 ± 0.036^{b}
R(1,43)	5725.71	16.75 ± 0.38^{a}	0.500 ± 0.025^{a}	12.05 ± 0.49^{b}	0.455 ± 0.037^{b}
R(1,44)	5891.27	16.45 ± 0.41^{a}	$0.480 \; \pm \; 0.026^{a}$	12.09 ± 0.48^{b}	0.478 ± 0.037^{b}
R(1,45)	6060.50	16.40 ± 0.46^{a}	$0.488 \; \pm \; 0.028^{a}$	11.55 ± 0.52^{b}	0.425 ± 0.038^{b}
R(1,46)	6233.39	16.22 ± 0.52^{a}	0.497 ± 0.031^{a}	11.57 ± 0.52^{b}	0.455 ± 0.039^{b}
R(1,47)	6409.92	16.31 ± 0.60^{a}	0.501 ± 0.034^{a}	11.37 ± 0.59^{b}	0.429 ± 0.040^{b}
R(1,48)	6590.11	15.72 ± 0.64^{c}	0.465 ± 0.046^{c}	$11.26 \pm 0.66^{\circ}$	0.429 ± 0.065^{c}
R(1,49)	6773.93	15.51 ± 0.71^{c}	0.456 ± 0.045^{c}	11.10 ± 0.71^{c}	0.422 ± 0.064^{c}
R(1,50)	6961.38	15.30 ± 0.79^{c}	$0.448~\pm~0.045^{c}$	10.94 ± 0.76^{c}	$0.414 \pm 0.063^{\circ}$
R(1,51)	7152.46	15.09 ± 0.88^{c}	0.439 ± 0.044^{c}	10.78 ± 0.82^{c}	0.406 ± 0.062^{c}
R(1,52)	7347.15	$14.89 \pm 0.98^{\circ}$	$0.431 \pm 0.043^{\circ}$	$10.62 \pm 0.88^{\circ}$	0.398 ± 0.061^{c}
R(1,53)	7545.45	14.53 ± 1.13^{b}	0.431 ± 0.037^{b}	10.47 ± 0.94^{c}	$0.390 \pm 0.060^{\circ}$
R(1,54)	7747.36	14.38 ± 1.19^{b}	0.383 ± 0.037^{b}	10.29 ± 0.98^{b}	0.401 ± 0.043^{b}
R(1,55)	7952.85	14.28 ± 1.40^{b}	0.401 ± 0.038^{b}	10.25 ± 1.12^{b}	0.393 ± 0.044^{b}
R(1,56)	8161.93	13.98 ± 1.40^{b}	0.372 ± 0.039^{b}	10.18 ± 1.23^{b}	0.379 ± 0.044^{b}
R(1,57)	8374.60	13.91 ± 1.64^{c}	$0.389~\pm~0.038^{c}$	9.88 ± 1.26^{c}	0.359 ± 0.056^{c}
R(1,58)	8590.82	13.53 ± 1.82^{b}	0.382 ± 0.041^{b}	10.00 ± 1.55^{b}	0.355 ± 0.045^{b}

- ^a Power law fit incorporates high-temperature gas cell data
- b Power law fit incorporates room-temperature broadening estimation (discussed in Section 4.1)
- ^c Interpolation based on J"-dependence (reference Fig. 9)

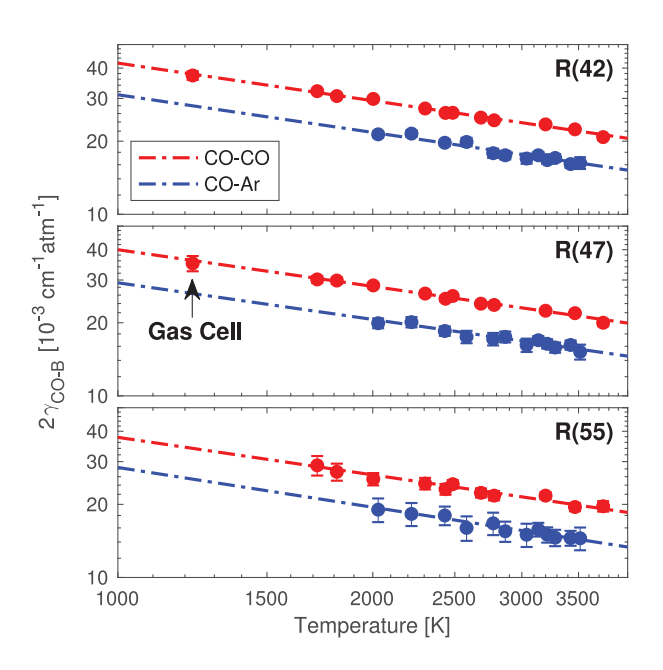
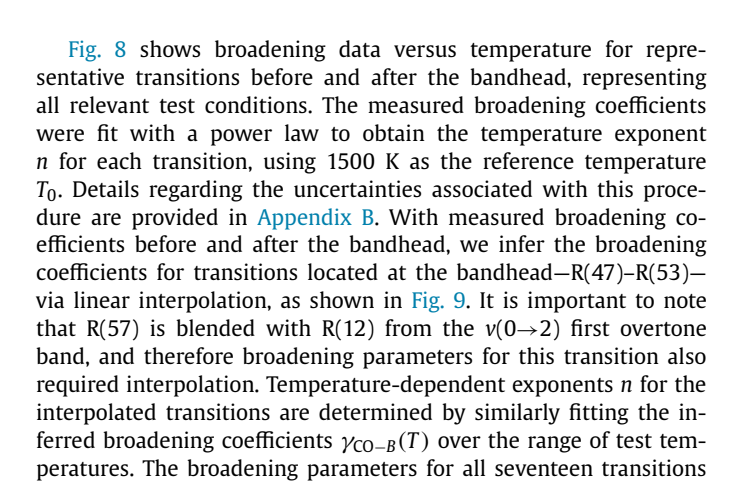


Fig. 8. CO- and Ar-broadening coefficients for select transitions with power law fits for 1000–4000 K. High-temperature optical cell data at 1226 K annotated, all other points from shock tube experiments.



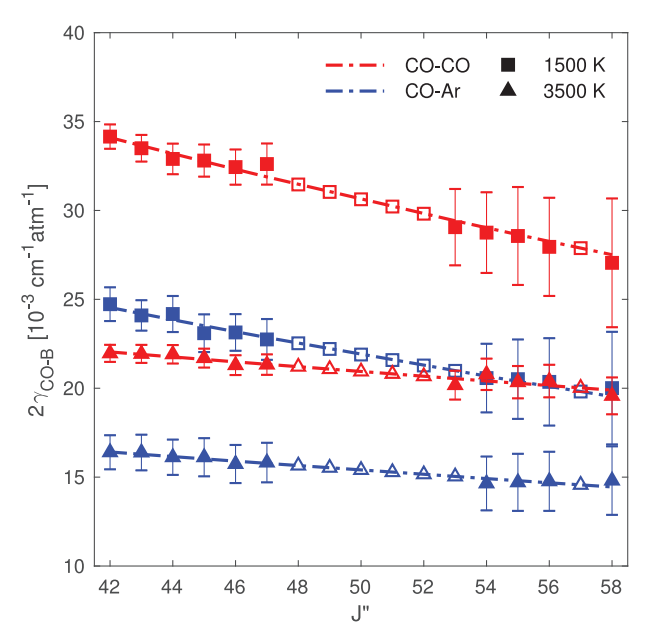


Fig. 9. Measured broadening coefficients $2\gamma_{\text{CO}-B}$ for J''=42-58 for CO and Ar at 1500 K and 3500 K. Least-squares exponential fits (dashed lines) of the measured broadening coefficients (filled markers) are used to estimate $2\gamma_{\text{CO}-B}$ for J'' too interfered to measure directly (open markers).

and their uncertainties are listed in Table 1. Subscripts in the table indicate if the reported parameter is an interpolated value or if it incorporates any high-temperature gas cell data or room-temperature estimations. Power-law fits of all measured broadening coefficients versus temperature (similar to the subset shown in Fig. 8) are provided in the Supplementary Material.

4.2. Line mixing

As discussed in Section 2.2, the relaxation matrix, \mathbf{W} , accounts for the collisional rates that result in line mixing in the spectra. The real diagonal elements of \mathbf{W} are the broadening coefficients, γ_J , the imaginary diagonal elements are the pressure shifts, Δv_{0J} , the real off-diagonal elements represent the state-specific population transfer rates, $R_{J \to K}$, and the imaginary off-diagonal

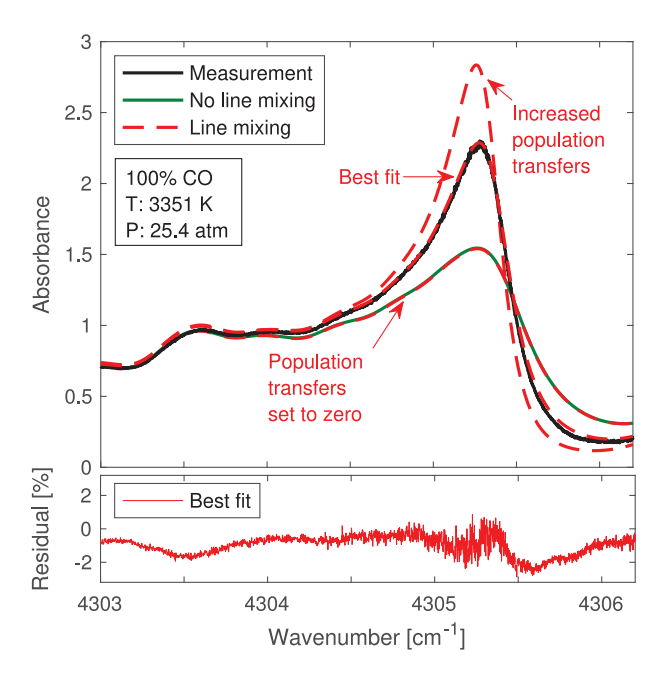


Fig. 10. Absorbance measurement of the $v(1\rightarrow 3)$ first overtone bandhead of CO at 3351 K and 25.4 atm with spectral simulations using Eq. (2) (green) and Eq. (7) (red) with no population transfers, too many population transfers, and best-fit population transfers.

components are set to zero. The reported broadening coefficients in Table 1 and the pressure shift coefficients from the HITEMP database [31] are used to complete the real and imaginary diagonal elements of W, respectively. The MEG law described by Eq. (17) is implemented to model the population transfer rates. To find the MEG law coefficients, a_i , high-pressure absorbance data measured using the shock tube facility are least-squares fit with the absorbance model, given by Eq. (7), with a_1 , a_2 , and a_3 set as the free parameters. It should be noted that since line mixing only occurs within the same vibrational band, as described in Section 2.2, transitions not belonging to the $v(1\rightarrow 3)$ first overtone hot band were simulated using the HITEMP database and removed from the measured absorbance data prior to the fitting routine. This procedure was initially carried out using pure CO in order to determine the population transfer rates associated with CO-CO collisions, and then repeated with test gas mixtures of 30% CO/Ar to obtain the appropriate rates for CO-Ar collisions using Eq. (16).

A comparison of representative high-pressure absorbance data collected in the shock tube at 25 atm and 3350 K is shown in Fig. 10 with various simulated results from the line mixing model. Without line mixing, the simulated spectra poorly represent the measured spectra near the bandhead, where most population transfers occur. Implementing the fitting routine described above allows for a high fidelity reconstruction of the spectra with a max residual < 3%. This compares to a disagreement of nearly 50% at the bandhead peak without accounting for line mixing. As expected, away from the bandhead, the line mixing model still agrees well with both the measured absorbance and the simulated spectra without any line mixing. Notably, with the MEG law coefficients established, we can adjust the a_1 parameter to vary the degree of line mixing and visualize the associated changes in the spectra. As population transfer rates increase, line mixing favors population transfers from weak absorption regions to strong absorption regions; consequently, narrowing the spectral structure and increasing the differential absorption near the bandhead.

It is informative to compare the transfer rates of different transitions as a function of ΔJ . Fig. 11 shows the rates for select

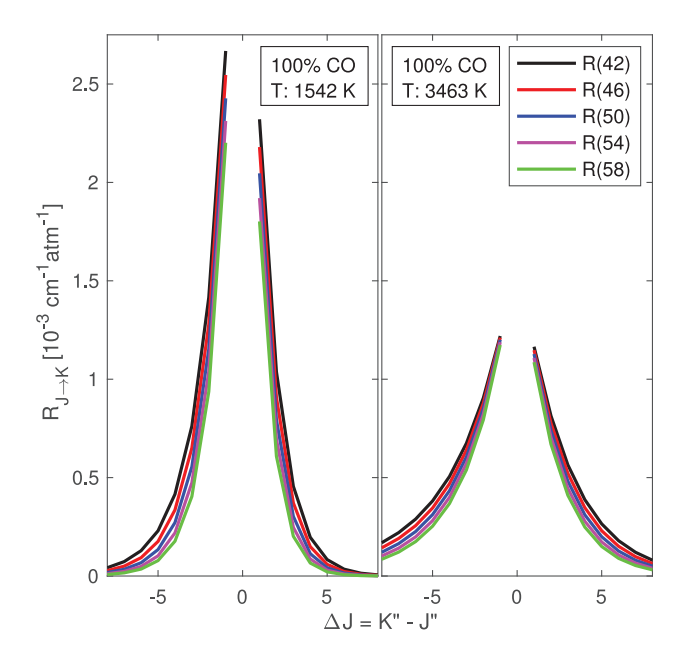


Fig. 11. Population transfer rates $R_{J \to K}$ given by the MEG model, from select initial states J'' = 42, 46, 50, 54, and 58 to final K'' states, plotted as $\Delta J = K'' - J''$.

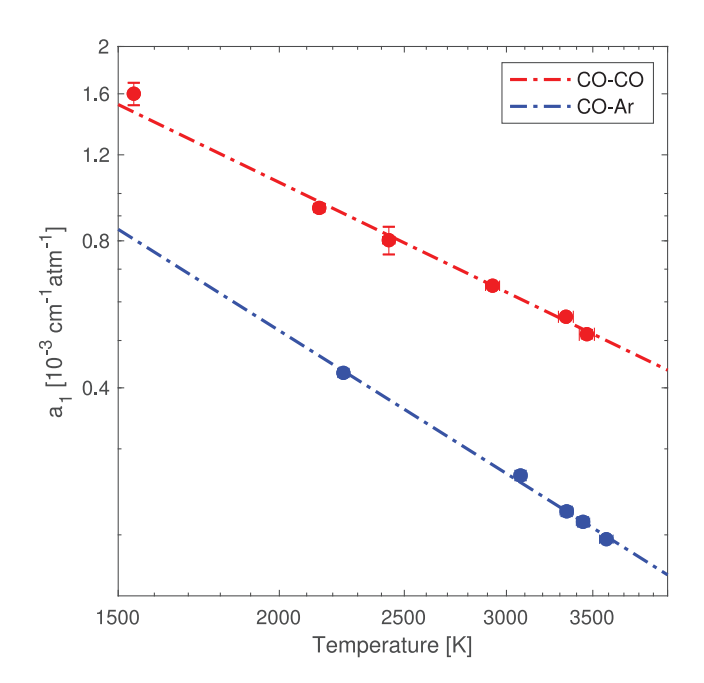
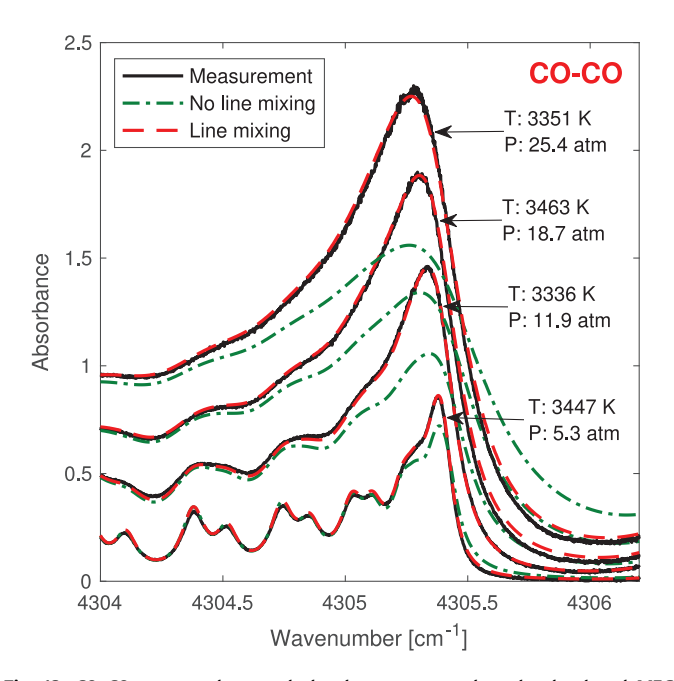


Fig. 12. Best-fit determinations of a_1 for different temperatures (markers) with power law fits (dashed lines) for both CO–CO and CO–Ar collisional line mixing.

transitions given by the line-mixing model at two conditions. Since collision-induced transfers across larger rotational levels require more energy, $R_{J \to K}$ decays as ΔJ increases. Accordingly, Fig. 11 illustrates that at higher temperatures, the population transfers from larger ΔJ become more significant. This can be described through Eqs. (11) and (17). It should be noted that the relaxation matrix scales linearly with pressure, but the relative probability of collision-induced transfers between a given ΔJ is only dependent on temperature. Previous studies have implemented the MEG model at room temperature and shown that collision transfer rates occur predominantly at $\Delta J = \pm 1$ [49,50]. However, at the high temperatures (> 1500 K) investigated in this work, population



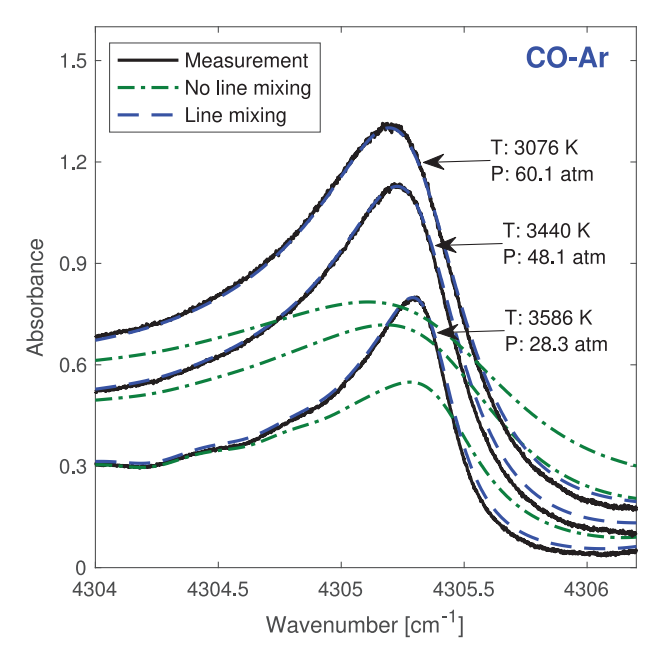


Fig. 13. CO–CO: measured spectral absorbance compared to the developed MEG model used to capture line-mixing effects over a range of pressures. The simulated spectral absorbance with no line mixing is illustrated for reference.

Fig. 14. CO–Ar: measured spectral absorbance compared to the developed MEG model used to capture line-mixing effects over a range of pressures. The simulated spectral absorbance with no line mixing is illustrated for reference.

Table 2Temperature-dependent MEG law parameters determined in this work.

	a ₁ (1500 K) [10 ⁻³ cm ⁻¹ atm ⁻¹]	a_2	a_3	a ₄	m
CO-CO CO-Ar	$\begin{array}{ccc} 1.52 \; \pm \; 0.15 \\ 0.85 \; \pm \; 0.13 \end{array}$	$\begin{array}{ccc} 0.51 \; \pm \; 0.05 \\ 0.30 \; \pm \; 0.04 \end{array}$	$\begin{array}{cccc} 5.21 \ \pm \ 0.10 \\ 7.46 \ \pm \ 0.15 \end{array}$	2 2	$\begin{array}{c} 1.28 \ \pm \ 0.06 \\ 1.66 \ \pm \ 0.09 \end{array}$

transfers with larger ΔJ significantly contribute to the population redistribution.

With the MEG law coefficients inferred empirically at various conditions, the temperature dependence of $a_1(T)$ was found through Eq. 19 by fitting experimental data at different temperatures, while holding a_2 and a_3 constant. The temperature dependence of the relaxation matrix is captured in Fig. 12 for both CO-CO and CO-Ar collisions. Notably, the temperature exponents for the off-diagonal components of the relaxation matrix are larger than those of the corresponding broadening coefficients. For CO-CO collisions, a_2 and a_3 were obtained at 3463 K and 18.7 atm with $a_1(T)$ reported at a reference temperature of 1500 K. Similarly, for CO-Ar collisions, a_2 and a_3 were obtained at 3586 K and 28.3 atm with $a_1(T)$ reported at a reference temperature of 1500 K. The reported MEG law coefficients can be found in Table 2. It is important to note that the specific transfer rates obtained by the reported MEG law coefficients do not in themselves sum up to the broadening coefficient (as shown in Eq. (15)) as there are other state-changing collisions not accounted for in the modeled absorbance. As such, caution should be exercised in using these inferred population transfer rates beyond modeling the target absorption spectra, as the absolute values have not been normalized.

With an established temperature dependence for $R_{J \to K}$ and γ_J , the full relaxation matrix can be calculated over a wide range of temperatures and pressures. To validate the pressure scalability of the line mixing model, a series of shock tube experiments were conducted from 5–25 atm for pure CO and 25–60 atm for 30% CO/Ar at similar temperatures, respectively, as shown in Figs. 13 and 14. At all pressures, the line mixing model exhibits

excellent agreement with the measured absorbance spectra. More specifically, in these figures, the a_i parameters were obtained at a single pressure and then used to calculate the spectra at the other pressures; therefore, validating the pressure scalability of the MEG law model. It should be noted that below 5 atm we found the simulated spectral shape could no longer accurately represent the measured spectra, a limit associated with the Lorentzian lineshape assumption in Eq. (7). An additional Voigt convolution step with the Gaussian function is required to capture the less prominent line mixing at lower pressures.

5. Conclusion

Self- and Ar-broadening coefficients and temperaturedependent exponents for CO have been measured and reported for 17 rovibrational transitions, R(42)–R(58), in the $v(1\rightarrow 3)$ first overtone hot band of CO near 2.3 µm. Experiments were conducted over a wide range of temperatures, 1200-3750 K, utilizing a shock tube facility and a heated gas cell. To the authors' knowledge, this work represents the first experimental study of these very high rotational energy transitions ($E'' = 5500-8600 \,\mathrm{cm}^{-1}$), extending the spectroscopic knowledge base of temperature-dependent broadening for CO. With broadening parameters established, a modified exponential gap model was developed to evaluate the thermodynamic scaling of state-specific collisional transfer rates associated with line mixing. The line-mixing model developed in this work quantitatively resolves the spectral domain over a range of extreme temperatures and pressures, 2000-3600 K and 5-60 atm, relevant to combustion and planetary entry.

Acknowledgements

This work was supported by the U.S. National Science Foundation, award no. 1752516, and by the Air Force Research Laboratory under award no. 16-EPA-RQ-09. FAB acknowledges support from the Eugene V. Cota-Robles Fellowship. DIP is supported in part by NSF AGEP award no. 1306683.

The authors acknowledge the experimental assistance of Kevin K. Schwarm in the optical gas cell measurements and Christopher C. Jelloian in the shock tube experiments. The authors also acknowledge the design, manufacturing, and testing efforts of Nicholas M. Kuenning and Anneliese R. Peterson for metal diaphragm components and tooling, supported by the NSF REU Program.

Appendix A. Unifying line mixing equations

Within the impact approximation, the absorption coefficient for overlapping lines can be written as:

$$k_{\nu} = \frac{N}{\pi} \operatorname{Im}(\mathbf{d} \cdot \mathbf{G}^{-1} \cdot \boldsymbol{\rho} \cdot \mathbf{d})$$
(A.1)

In this form, solving for k_{ν} can be significantly time consuming, especially if considering mixing between multiple transitions, as it requires a matrix inversion for each frequency. The computation of k_{ν} is simplified considerably by following the procedure discussed in Section 2.2, as shown by Gordon and McGinnis [30] and Koszykowski et al. [51]. The resulting expression for k_{ν} is shown in Eq. (A.2).

$$k_{\nu} = \frac{N}{\pi} \operatorname{Im} \left[\sum_{J} \frac{(\mathbf{d} \cdot \mathbf{A})_{J} (\mathbf{A}^{-1} \cdot \boldsymbol{\rho} \cdot \mathbf{d})_{J}}{(\nu - \omega_{J})} \right]$$
(A.2)

Note that Eq. A.2 is still an exact expression for k_{ν} and involves no approximations.

In this form, \mathbf{d} represents a vector of transition amplitudes with a temperature dependence given by:

$$d_{J} = \sqrt{\frac{S_{J}(T)}{\rho_{J}}} \tag{A.3}$$

where $S_J(T)$ [cm⁻¹/(molec · cm⁻²)] is the transition line strength and ρ_J is the Boltzmann population fraction given by Eq. (8). It is often of interest to express **d** in terms of temperature independent molecular properties. This can be done by letting $S_J(T)$ take the following form:

$$S_{J}(T) = I_{a} \frac{A_{J}}{8\pi c v_{0}^{2}} \frac{g_{J}' \exp\left(-\frac{hcE_{J}''}{k_{B}T}\right) \left[1 - \exp\left(-\frac{hcv_{0}}{k_{B}T}\right)\right]}{Q}$$
(A.4)

where I_a is the natural terrestrial isotopic abundance, g_j' is the upper state degeneracy, E_j'' [cm⁻¹] is the lower state energy, Q is the total internal partition function, and A_J [s⁻¹] is the Einstein coefficient for spontaneous emission. The Einstein-A coefficient is independent of temperature and, for electric dipole transitions, can be related to the weighted transition-moment squared \mathfrak{R}_J^2 [Debye²] through Eq. (A.5):

$$A_{J} = \frac{64\pi^{4}}{3h} v_{0}^{3} \frac{g_{J}^{"}}{g_{J}^{"}} \mathfrak{R}_{J}^{2}$$
(A.5)

where $g_J^{\prime\prime}$ is the lower state degeneracy. Substituting Eq. (A.5) into Eq. (A.4) yields:

$$S_J(T) = I_a \frac{8\pi^3}{3hc} \nu_0 \rho_J \left[1 - \exp\left(-\frac{hc\nu_0}{k_B T}\right) \right] \Re_J^2$$
 (A.6)

Finally, combining Eq. (A.2) with Eqs. (A.5) and (A.6) produces an expression for absorption coefficient accounting for line mixing frequently seen in literature:

$$k_{\nu} = I_{a} \frac{8\pi^{2}}{3hc} \nu \left[1 - \exp\left(-\frac{hc\nu}{k_{B}T}\right) \right]$$

$$\times \sum_{J} \sum_{K} N_{J} \mathfrak{R}_{J} \mathfrak{R}_{K}$$

$$\times \operatorname{Im}\{\langle \langle J | [\mathbf{\Sigma} - \mathbf{L_{0}} - iP\mathbf{W}]^{-1} | K \rangle \rangle\}$$
(A.7)

where Σ , L_0 , and W are operators in Liouville line space. Σ and L_0 are diagonals associated with the wavenumber of the calculation ν and the transition line center ν_0 , respectively. All collisional influences on spectral shape are contained in the relaxation matrix W, as discussed in Section 2.2.

Appendix B. Uncertainty analysis

The broadening parameters reported in Table 1 and the MEG law coefficients reported in Table 2 are provided with uncertainty estimates, the calculations of which are detailed in this Appendix. Unless otherwise noted, we follow the Taylor series method (TSM) of uncertainty propagation [52], in which the uncertainty of a variable r, Δr , is given by:

$$(\Delta r)^2 = \left(\frac{\partial r}{\partial x_1} \Delta x_1\right)^2 + \left(\frac{\partial r}{\partial x_2} \Delta x_2\right)^2 + \cdots$$
 (B.1)

where x_i are dependent variables and Δx_i are their respective uncertainties.

B1. Thermodynamic state variables

The parameters we report are determined from measurements made at various thermodynamic conditions, uncertainties of which ultimately affect the temperature- and pressure-dependence of the associated models.

Uncertainty in pressure, ΔP is generally dominated by two sources. For both shock tube and heated optical cell experiments, uncertainty in the pressure transducer/capacitance manometer measurements ΔP_{meas} leads to uncertainties in broadening parameters. For the shock tube experiments, uncertainty in the reflected shock pressure P_5 due to uncertainties associated with the shock relations ΔP_5 contribute.

$$\left(\frac{\Delta P}{P}\right)^2 = \left(\frac{\Delta P_{meas}}{P_{meas}}\right)^2 + \left(\frac{\Delta P_5}{P_5}\right)^2 \tag{B.2}$$

For the heated optical static gas cell experiments, ΔP_5 is taken to be zero, and ΔP_{meas} is 0.012% of the measurement reported by the capacitance manometer, while for the shock tube experiments, ΔP_{meas} is 0.18% of the measurement reported by the pressure transducer.

Uncertainty in temperature, ΔT , is different for each of the devices. For the shock tube measurements, the uncertainty in temperature is simply the uncertainty in reflected shock temperature T_5 , ΔT_5 . For the sake of brevity, the uncertainties ΔP_5 and ΔT_5 will not be discussed here in further detail; however, we note that significant contributors include uncertainties in the composition of the driven gas (from the barometric mixture preparation), uncertainties in the time-of-arrival measurements, and small uncertainties in the initial pressure P_1 and temperature T_1 . Further information regarding uncertainties in reflected shock conditions can be found in the work by Campbell et al. [42].

Temperature uncertainty in the static optical cell measurements taken at 1226 K is $\Delta T_{meas} = 10$ K, based on the uncertainty of thermocouple measurements taken on the outside surface of the cell.

More detail about the optical cell used in this paper is provided in previous research [41].

B2. Broadening coefficient

The uncertainties in collisional broadening coefficient (for absorber A by perturber B) $\gamma_{A-B}(T_0)$, $\Delta\gamma_{A-B}(T_0)$, and temperature-dependent exponent n, Δn , are determined from applying a linear regression to Eq. (6). In this case, the standard errors of the slopes and intercepts of the fitted lines are Δn and $\Delta\gamma_{A-B}(T_0)$, respectively. In our linear regressions, we follow the approach of York et al. [53], incorporating variable uncertainties in both x and y to provide slope and intercept standard errors more reflective of variable measurement quality amongst the data. In practice, this allows for us to utilize measurements from both the shock tube and the heated static optical cell in the same regression (as shown in Fig. 8), despite that each of these devices has different measurement uncertainties in thermodynamic state variables.

 $\Delta \gamma_{A-B}(T_0)$ and Δn thus have uncertainty dependence on ΔT (discussed previously) and $\Delta \gamma_{A-B}(T)$. We can determine $\Delta \gamma_{A-B}(T)$ by applying Eq. (B.1) to Eq. (5) after rearranging to solve for $\gamma_{A-B}(T)$:

$$\left(\frac{\Delta \gamma_{A-B}(T)}{\gamma_{A-B}(T)}\right)^{2} = \left(\frac{\Delta(\Delta \nu_{C})}{2PX_{B}}\right)^{2} + \left(\frac{\Delta \nu_{C} \Delta P}{2P^{2}X_{B}}\right)^{2} + \left(\frac{\Delta \nu_{C} \Delta X_{B}}{2PX_{B}^{2}} - \frac{\Delta X_{B}}{X_{B}} \sum_{C} X_{C} \gamma_{A-C}(T)\right)^{2} + \left(\frac{1}{X_{B}} \sum_{C} \Delta X_{C} \gamma_{A-C}(T)\right)^{2} + \left(\frac{1}{X_{B}} \sum_{C} X_{C} \Delta \gamma_{A-C}(T)\right)^{2} \tag{B.3}$$

Eq. (B.3) describes the uncertainty dependence of the broadening coefficient of absorber A by perturber B, $\gamma_{A-B}(T)$, on the uncertainties in collisional width Δv_C , total pressure P, mole fraction of perturber B, X_B , and broadening influences of any other perturbers C (which includes self-broadening by A). For self-broadening, $X_B = X_A \approx 1$ and $X_C = 0$, and so the last few terms of Eq. (B.3) drop out. When considering only a single perturber B, C = A to account for the influence of self-broadening. ΔP is given by Eq. (B.2), and mole fraction uncertainties ΔX_i are determined based on the barometric mixture preparation uncertainties. Collisional width Δv_C is determined from a Voigt fit of the measured absorbance spectra, and so $\Delta(\Delta v_C)$ is conservatively estimated by multiplying the maximum residual of the Voigt fit by Δv_C , typically less than 3%.

Thus, the uncertainty dependencies of $\Delta\gamma_{A-B}(T_0)$ and Δn are all accounted for. Some sensitivity is observed in the preceding equations regarding the mole fraction of perturber B, such that lower mole fractions of B lead to higher uncertainties in $\Delta\gamma_{A-B}(T)$ for a given transition, as demonstrated in Figs. 8 and 9.

B3. MEG law coefficients

Because the MEG law is an empirical model [34,35], the coefficients $a_1(T)$, a_2 , and a_3 for each experiment are determined by a nonlinear least-squares fit, and so their uncertainties cannot be interpreted as meaningfully through physical relationships as described by Eq. (B.1). Thus, we estimate uncertainties for this model in a manner consistent with how the model will be used; i.e., to make predictions of absorption spectra in the range of thermodynamic conditions described in this work. The uncertainties in $a_1(T)$,

 a_2 , and a_3 for each high-pressure shock tube experiment were determined by varying the wavenumber range over which the least-squares fit described in Section 4.2 was made. The differences between the values of a_i determined from the simulating the wavelength range of the measured experiment (4300–4310 cm $^{-1}$) and the values of a_i determined from simulating the wavelength range of the entire $v(1\rightarrow 3)$ band (4210–4310 cm $^{-1}$) were taken to be a conservative estimate of Δa_i . This represents the uncertainty associated with using experimental data gathered from a limited spectral range to model the line mixing behavior of the entire band.

The uncertainties for $a_1(T)$, $\Delta a_1(T)$, are shown as error bars in Fig. 12. Together with ΔT , these are used in the linear regression determination of $a_1(T_0)$ and m to obtain their respective uncertainties $\Delta a_1(T_0)$ and Δm using the same approach of York et al. [53] as described for $\Delta \gamma_{A-B}(T_0)$ and Δn .

 Δa_i are observed to be similar for line-mixing in argon despite the lower signal-to-noise ratios in the measurements; this is because the MEG law coefficients a_i determined for pure CO are used to determine a_i for argon through Eq. (16). Since these coefficients are treated as fixed for this second least-squares fitting procedure, the additional constraints on the fit reduce the variation in suitable a_i . As such, the MEG law coefficients presented in Table 2 for CO–Ar should not be interpreted independently from those for CO–CO.

Supplementary material

Supplementary material associated with this article can be found, in the online version, at doi:10.1016/j.jqsrt.2019.106636.

References

- Stephens RD, Cadle SH. Remote sensing measurements of carbon monoxide emissions from on-road vehicles. J Air & Waste ManagAssoc 1991;41(1):39–46. doi:10.1080/10473289.1991.10466823.
- [2] Fishman J, Bowman KW, Burrows JP, Richter A, Chance KV, Edwards DP, et al. Remote sensing of tropospheric pollution from space. Bull Am Meteorol Soc 2008;89(6):805–22. doi:10.1175/2008BAMS2526.1.
- [3] Spearrin RM, Goldenstein CS, Schultz IA, Jeffries JB, Hanson RK. Simultaneous sensing of temperature, CO, and CO₂ in a scramjet combustor using quantum cascade laser absorption spectroscopy. Appl Phys B 2014;117(2):689–98. doi:10. 1007/s00340-014-5884-0.
- [4] Howell JR, Siegel R, Mengüç MP. Thermal radiation heat transfer. 5th. Boca Raton, FL: CRC Press; 2011.
- [5] Sur R, Sun K, Jeffries JB, Hanson RK. Multi-species laser absorption sensors for in situ monitoring of syngas composition. Appl Phys B 2014;115(1):9–24. doi:10.1007/s00340-013-5567-2.
- [6] Chao X, Jeffries JB, Hanson RK. Absorption sensor for CO in combustion gases using 2.3 μm tunable diode lasers. Meas Sci Technol 2009;20(11):115201. doi:10.1088/0957-0233/20/11/115201.
- [7] Lee DD, Bendana FA, Schumaker SA, Spearrin RM. Wavelength modulation spectroscopy near 5 µm for carbon monoxide sensing in a high-pressure kerosene-fueled liquid rocket combustor. Appl Phys B 2018;124(5):77. doi:10. 1007/s00340-018-6945-6.
- [8] Bendana FA, Lee DD, Spearrin RM, Schumaker SA, Danczyk SA. Infrared laser absorption thermometry and CO sensing in high-pressure rocket combustion flows from 25 to 105 bar. In: AIAA Scitech 2019 Forum. Reston, Virginia: American Institute of Aeronautics and Astronautics; 2019. p. 1–8. ISBN 978-1-62410-578-4. doi:10.2514/6.2019-1610.
- [9] Hartmann J-M, Tran H, Armante R, Boulet C, Campargue A, Forget F, et al. Recent advances in collisional effects on spectra of molecular gases and their practical consequences. J Quant Spectrosc Radiat Transf 2018;213:178–227. doi:10.1016/j.iasrt.2018.03.016.
- [10] Sinclair P, Duggan P, Berman R, Drummond JR, May A. Line broadening in the fundamental band of CO in CO-He and CO-Ar mixtures. J Mol Spectrosc 1998;191(2):258-64. doi:10.1006/jmsp.1998.7628.
- [11] Zou Q, Varanasi P. New laboratory data on the spectral line parameters in the 1-0 and 2-0 bands of ¹²C¹⁶O relevant to atmospheric remote sensing. J Quant Spectrosc Radiat Transf 2002;75(1):63–92. doi:10.1016/S0022-4073(02) 00007-9
- [12] Ren W, Farooq A, Davidson DF, Hanson RK. CO concentration and temperature sensor for combustion gases using quantum-cascade laser absorption near 4.7 µm. Appl Phys B 2012;107(3):849–60. doi:10.1007/s00340-012-5046-1.
- [13] Predoi-Cross A, Bouanich JP, Benner DC, May AD, Drummond JR. Broadening, shifting, and line asymmetries in the 2←0 band of CO and CO-N₂: Experimental results and theoretical calculations. J Chem Phys 2000;113(1):158-68. doi:10.1063/1.481783.

- [14] Bouanich J-P. On the temperature dependence of self-broadening in the first overtone band of CO. J Quant Spectrosc Radiat Transfer 1984;31(6):561–7. doi:10.1016/0022-4073(84)90061-X.
- [15] BelBruno JJ, Gelfand J, Radigan W, Verges K. Helium and self-broadening in the first and second overtone bands of 12C160. J Mol Spectrosc 1982;94(2):336– 42. doi:10.1016/0022-2852(82)90009-1.
- [16] Devi V, Benner D, Smith M, Rinsland C, Mantz A. Determination of self- and H₂-broadening and shift coefficients in the 2-0 band of ¹²C¹⁶O using a multi spectrum fitting procedure. J Quant Spectrosc Radiat Transf 2002;75(4):455– 71. doi:10.1016/S0022-4073(02)00023-7.
- [17] Malathy Devi V, Chris Benner D, Smith M, Mantz A, Sung K, Brown L, et al. Spectral line parameters including temperature dependences of self- and airbroadening in the 2←0 band of CO at 2.3 μm. J Quant Spectrosc Radiat Transf 2012;113(11):1013–33. doi:10.1016/j.jqsrt.2012.02.010.
- [18] Hunt RH, Toth RA, Plyler EK. High resolution determination of the widths of self broadened lines of carbon monoxide. J Chem Phys 1968;49(9):3909–12. doi:10.1063/1.1670699.
- [19] Wöjtewicz S, Stec K, Masłowski P, Cygan A, Lisak D, Trawiński R, et al. Low pressure line-shape study of self-broadened CO transitions in the (3←0) band. J Quant Spectrosc Radiat Transf 2013;130:191–200. doi:10.1016/j.jqsrt.2013.06. 005.
- [20] Predoi-Cross A, Hnatovsky C, Strong K, Drummond J, Chris Benner D. Temperature dependence of self- and N₂-broadening and pressure-induced shifts in the 3←0 band of CO. J Mol Struct 2004;695–696:269–86. doi:10.1016/j.molstruc. 2003.12.043.
- [21] Kowzan G, Stec K, Zaborowski M, Wójtewicz S, Cygan A, Lisak D, et al. Line positions, pressure broadening and shift coefficients for the second overtone transitions of carbon monoxide in argon. J Quant Spectrosc Radiat Transf 2017;191:46–54. doi:10.1016/j.jqsrt.2016.12.035.
- [22] Malathy Devi V, Chris Benner D, Smith MAH, Mantz AW, Sung K, Brown LR. Spectral line parameters including temperature dependences of air-broadening for the 2←0 bands of 13C16O and 12C18O at 2.3 μm. J Mol Spectrosc 2012;276–277:33–48. doi:10.1016/j.jms.2012.05.005.
- [23] Hartmann JM, Boulet C, Robert D. Collisional effects on molecular spectra. Elsevier; 2008. ISBN 9780444520173. doi:10.1016/B978-0-444-52017-3.X0001-5.
- [24] Hanson RK, Spearrin RM, Goldenstein CS. Spectroscopy and optical diagnostics for gases. Springer; 2016. ISBN 978-3-319-23252-2. doi:10.1007/978-3-319-23252-2.
- [25] Hill TL. An introduction to statistical thermodynamics. Addison-Wesley Publishing Co; 1960. ISBN 9780486652429.
- [26] Fano U. Pressure broadening as a prototype of relaxation. Phys Rev 1963;131(1):259–68. doi:10.1103/PhysRev.131.259.
- [27] Baranger M. Problem of overlapping lines in the theory of pressure broadening. Phys Rev 1958;111(2):494–504. doi:10.1103/PhysRev.111.494.
- [28] Pine AS, Looney JP. Self broadening and line mixing in HCN Q branches. J Chem Phys 1992;96(3):1704–14. doi:10.1063/j.462125.
- [29] Strow LL, Reuter D. Effect of line mixing on atmospheric brightness temperatures near 15 μm. Appl Opt 1988;27(5):872. doi:10.1364/AO.27.000872.
- [30] Gordon RG, McGinnis RP. Line shapes in molecular spectra. J Chem Phys 1968;49(5):2455–6. doi:10.1063/1.1670429.
- [31] Gordon I, Rothman L, Hill C, Kochanov R, Tan Y, Bernath P, et al. The HI-TRAN2016 molecular spectroscopic database. J Quant Spectrosc Radiat Transf 2017;203:3-69. doi:10.1016/j.jqsrt.2017.06.038.
- [32] Gordon RG. Semiclassical theory of spectra and relaxation in molecular gases. J Chem Phys 1966;45(5):1649–55. doi:10.1063/1.1727808.
- [33] Boissoles J, Boulet C, Robert D, Green S. State to state rotational phase coherence effect on the vibration rotation band shape: an accurate quantum calculation for CO–He. J Chem Phys 1989;90(10):5392–8. doi:10.1063/1.456688.

- [34] Koszykowski ML, Rahn LA, Palmer RE, Coltrin ME. Theoretical and experimental studies of high-resolution inverse Raman spectra of molecular nitrogen at 1–10 atm. J Phys Chem 1987;91(1):41–6. doi:10.1021/i100285a012.
- [35] Rahn L, Palmer R, Koszykowski M, Greenhalgh D. Comparison of rotationally inelastic collision models for Q-branch Raman spectra of N₂. Chem Phys Lett 1987;133(6):513–16. doi:10.1016/0009-2614(87)80069-6.
- [36] Hirschfelder JO, Curtiss CF, Bird RB. Molecular theory of gases and liquids. 2nd. New York: John Wiley & Sons, Inc.; 1964.
- [37] Rosasco GJ, Rahn LA, Hurst WS, Palmer RE, Dohne SM. Measurement and prediction of Raman Q branch line self broadening coefficients for CO from 400 to 1500 K. J Chem Phys 1989;90(8):4059–68. doi:10.1063/1.455764.
- [38] Looney J, Rosasco G, Rahn L, Hurst W, Hahn J. Comparison of rotational relaxation rate laws to characterize the Raman Q-branch spectrum of CO at 295 K. Chem Phys Lett 1989;161(3):232–8. doi:10.1016/S0009-2614(89)87066-6.
- [39] Ben-Reuven A. Impact broadening of microwave spectra. Phys Rev 1966;145(1):7–22. doi:10.1103/PhysRev.145.7.
- [40] Steinfeld JI, Ruttenberg P, Millot G, Fanjoux G, Lavorel B. Scaling laws for inelastic collision processes in diatomic molecules. J Phys Chem 1991;95(24):9638–47. doi:10.1021/j100177a010.
- [41] Schwarm KK, Dinh HQ, Goldenstein CS, Pineda DI, Spearrin RM. High-pressure and high-temperature gas cell for absorption spectroscopy studies at wavelengths up to 8 µm. J Quant Spectrosc Radiat Transf 2019;227:145–51. doi:10.1016/j.jqsrt.2019.01.029.
- [42] Campbell MF, Owen KG, Davidson DF, Hanson RK. Dependence of calculated postshock thermodynamic variables on vibrational equilibrium and input uncertainty. J Thermophys Heat Transf 2017;31(3):586–608. doi:10.2514/1.T4952.
- [43] Li H, Owens ZC, Davidson DF, Hanson RK. A simple reactive gasdynamic model for the computation of gas temperature and species concentrations behind reflected shock waves. Int J Chem Kinet 2008;40(4):189–98. doi:10.1002/kin. 20305
- [44] Millikan RC, White DR. Systematics of vibrational relaxation. J Chem Phys 1963;39(12):3209–13. doi:10.1063/1.1734182.
- [45] Rothman L, Gordon I, Barber R, Dothe H, Gamache R, Goldman A, et al. HITEMP, The high-temperature molecular spectroscopic database. J Quant Spectrosc Radiat Transf 2010;111(15):2139–50. doi:10.1016/j.jqsrt.2010.05.001.
- [46] Varghese PL, Hanson RK. Collisional narrowing effects on spectral line shapes measured at high resolution. Appl Opt 1984;23(14):2376. doi:10.1364/AO.23. 002376
- [47] Hartmann JM, Rosenmann L, Perrin MY, Taine J. Accurate calculated tabulations of CO line broadening by H₂O, N₂, O₂, and CO₂ in the 200-3000-K temperature range. Appl Opt 1988;27(15):3063. doi:10.1364/AO.27.003063.
- [48] Bouanich J-P, Haeusler C. Linewidths of carbon monoxide self-broadening and broadened by argon and nitrogen. J Quant Spectrosc Radiat Transfer 1972;12(4):695–702. doi:10.1016/0022-4073(72)90177-X.
- [49] Romanini D, Lehmann KK. Line mixing in the 106←000 overtone transition of HCN. J Chem Phys 1996;105(1):81–8. doi:10.1063/1.471883.
- [50] Wu J, Huang R, Gong M, Saury A, Carrasquillo M E. Rotational energy transfer in highly vibrationally excited HCN. J Chem Phys 1993;99(9):6474–82. doi:10. 1063/1.465865.
- [51] Koszykowski ML, Farrow RL, Palmer RE. Calculation of collisionally narrowed coherent anti-Stokes Raman spectroscopy spectra. Opt Lett 1985;10(10):478. doi:10.1364/OL.10.000478.
- [52] Coleman HW, Steele WG. Experimentation, validation, and uncertainty analysis for engineers. 3rd. Hoboken, NJ, USA: John Wiley & Sons, Inc.; 2009.
- [53] York D, Evensen NM, Martíez ML, De Basabe Delgado J. Unified equations for the slope, intercept, and standard errors of the best straight line. Am J Phys 2004;72(3):367–75. doi:10.1119/1.1632486.